Lung Cancer Detection: Advancing CT Image Analysis Through Hybrid Bidirectional Long Short-Term Memory and Recurrent Neural Network

Geetha Paranjothi1*, Dr. Arunachalam A.S.²

1* Research Scholar, Department of Computer Science, School of Computing Sciences, Vels Institute of Science, Technology and Advanced Studies (VISTAS), Tamil Nadu, India.

2Professor, Department of Computer Science, School of Computing Sciences, Vels Institute of Science, Technology and Advanced Studies (VISTAS), Tamil Nadu, India.

1*Corresponding Author Email: geethaocp@gmail.com

ARTICLE INFO	ABSTRACT
	Globally, lung cancer (LC) is the leading cause of death from cancer. Medical image analysis based on deep learning (DL) has strong potential for detecting and diagnosing lung cancer by identifying early symptoms with image aid from positron emission tomography (PET) and computed tomography (CT). The majority of DL models created for LC detection are very resource-intensive, requiring a great deal of computational capacity; hence, they pose a challenge to deployment on a standard clinical system and are therefore significantly less accessible in resource-constrained settings. This additional computational load may delay diagnosis and treatment, thus affecting the outcome of the patients. Therein lies the critical need for developing more lightweight and efficient deep learning models that ensure high accuracy while reducing computational requirements. This manuscript presents a Lung Cancer Detection technique, LCD-CT-BiLSTM-RNN, based on advanced CT image analysis. First, noise reduction in the lung CT images by anisotropic guided filtering (AGF) is performed. Then, adaptive fuzzy K-means clustering (AFKMC) separates the affected areas of cancer, and Synchroextracting Transform (SET) adds the spectral features. Finally, a hybrid BiLSTM and RNN architecture runs the classification task with an improved overall accuracy. Hybrid optimization using Slime Mould Optimization (SMO) and Golden Eagle Optimization (GEO) fine-tunes the model. The performance of the methods is assessed using MATLAB's accuracy, precision, recall, F1-score, specificity, Matthews Correlation Coefficient (MCC), and ROC to compare the acquired findings with the existing approaches. The performance of the proposed method provides 2.03%, 3.45%, and 2.36% higher accuracy compared with existing techniques like Fuzzy Particle Swarm Optimization with Convolutional Neural Network for Detection of LC (FPSO-CNN), Deep learning Instantaneously Accomplished Neural Network with Improved Profuse Clustering Technique for LC detection (DITNN-IPCT), and Residual Learning Denoising Model with Convolutional Neural Network (DR-Net-CNN) for the Detection of LC. **Keywords:** Lung cancer (LC), Deep learning (DL), Positron Emission Tomography (PET), Computed Tomography (CT), Guided Filtering, Fuzzy Means Clustering, Optimization Algorithm.

INTRODUCTION

Human genetic cells' (DNA) structure and function vary as a result of lifestyle changes [1]. Splitting the altered DNA produces duplicate DNA, which is then used to replace the damaged or mutated DNA when two new cells are formed [2]. Mutation is the term used to describe the process [where the altered DNA is split into two new cells [3]. The improper mutation of DNA cells typically results in the beginning of cancer because several factors influence the mutation process, including drinking patterns, smoking, radon gas exposure, and asbestos fiber inhalation [4]. The North American Association of Central Cancer Registries did an analysis (NNACCR) that predicts that 234,030 Americans will be affected by lung cancer in 2018. Lung cancer affects 13% of women and 14% of men in the United States [5]. Furthermore, 154,050 deaths out of 234,030 worldwide were determined to be fatal [6]. Based on the NNACCR report, LC is among the deadliest illnesses and has several symptoms including breathing difficulties, bloody coughing, chest pain, voice abnormalities, and voice loss [7]. Other symptoms that may indicate lung cancer include self-reported joint problems, memory loss, cachexia, weight loss, headaches, bleeding, neurological problems, blood clots, and facial edema [8]. Clinical physicians have investigated these signs using a spirometer, which gauges air intake and aids in the identification of lung cancer by employing several screening methods, such as genetic testing, liquid biopsy, bronch scope, reflex testing, and biopsy [9]. Lung cancer can be identified by biopsies, but maintaining precision and accuracy is challenging. Consequently, to study the adjustments made to the

body, computed tomography (CT) scans are performed using X-rays. A liquid or dye is put to the chest during this procedure, and the body is scanned for 10 to 30 minutes to take images [10]. Comparatively speaking to other imaging methods like MRI and PET, CT provides more information about the damaged portion during analysis since it repeatedly examines the soft tissues of the lung and organs [11]. Lung cancer prediction has benefited from screening methodology, although accuracy and early cancer detection are challenging to maintain [12]. Therefore, the clinical center must use the computer-assisted automated detection (CAD) [13] method to develop an efficient cancer prediction [14] system that makes use of an innovative and efficient method.

The inspection of the body's internal details, the restoration of details, the extraction of useful information, and the development of an informed approach for the identification of lung cancer all use the optimum lung image processing techniques [15]. Several processes are involved in processing approaches [16], including preprocessing lung images, segmentation of afflicted parts, extraction of features, and prediction of lung cancer. Because the technique analyzes each pixel in the lung image and divides the connected cells in the injured area, segmentation plays a critical function among the several stages in determining whether a condition is cancerous or not. Region segmentation is accomplished using several techniques, such as distributed clustering, Sobel, self-organizing maps, fuzzy c-means, k-means, Hopfield neural networks, and algometric clustering [17]. Canny edge detection techniques are used to predict the impacted zone. Additionally, several optimization techniques, such as the firefly algorithm, ant colony, genetic algorithm, and particle swarm optimization approach, are used to improve the clustering process. [18]. From the segmented lung region, a variety of features are extracted, including robust, statistical, and spectral properties, as well as local binary patterns. Support vector machines, an efficient machine learning technique, and a DL, which uses the data to train the CAD system in light of the requirement for the incoming fresh tests to be approved without any failures, are then used to handle these features [19]. Although the CAD system has efficient use of optimized methodologies, the complexity occasionally brought on by the big collection of lung images can lower the accuracy of cancer prediction [20]. Various picture coordinates have been used to assess the measurement of precision. Entropy is often identified using two methods, with the uniform sections of the image being examined with low-frequency values.

Lung cancer identification using CT image analysis is an important aspect in connection with its early diagnosis and treatment. Most available methods are characteristically associated with low prediction accuracy and result in high computational time, making them ineffective for practical applications in a clinical setup. The current methods for the use of CT imaging in the identification of LC often lack sufficient prediction accuracy, thus leading to misdiagnosis or delayed initiation of treatment. These methods are computationally very intensive and hence may not support real-time or near-real-time diagnosis easily, more so in resource-constraint situations. Motivated by these observations, in this research work, a new strategy is presented, referred to as LCD-CT-BiLSTM-RNN, incorporating state-of-the-art methods, viz. AGF for reducing noise, AFKMC for accurate segmentation, and SET to extract all-important features for enhancing both prediction accuracy and computational efficiency. This makes it easier to diagnose lung cancer with CT scans in a timely and reliable manner.

The major contributions of the manuscript are as follows,

- Anisotropic guided filtering is implemented to take off noise effectively while preserving the edges and hence improving the quality of the lung CT images.
- Uses adaptive fuzzy K-means clustering (AFKMC) for more flexible and precise segmentation of cancer-affected regions.
- Determines multiple spectral features from the segmented regions using Synchro Extracting Transform (SET) to capture indispensable patterns of data.
- A design in which BiLSTM and RNN architectures are combined to harness contextual information toward boosting classification accuracy of lung cancer.
- Incorporates Slime Mould Optimization and Golden Eagle Optimization in tuning model parameters, which help in improved overall performance.

This is way the remaining manuscript is arranged: The relevant studies is presented in Section 2, the suggested approach is presented in Section 3, the results and explanations are shown in Section 4, and the manuscript is concluded in Section 5.

RECENT RESEARCH WORK: A BRIEF REVIEW

Among the numerous research work on LC prediction using DL, the most recent research work is discussed in this section,

In 2020, Asuntha, et.al., [21] have suggested the classification and detection of LC using DL techniques. From input lung images, the system detects the cancerous lung nodules and categorizes the lungs with cancer based on the severity of the disease. Cancerous lung nodules were detected using deep learning techniques. The following advanced feature extraction techniques are applied: Zernike Moment, Local Binary Pattern, Scale Invariant Feature Transform, Wavelet transform-based features, and Histogram of Oriented Gradients. These extracted features were then passed through the FPSO algorithm to select the best features. These selected features were used for classification with deep learning techniques. Here, an FPSO-CNN was developed which may reduce the computational complexity of traditional CNN. Also, another dataset from Arthi Scan Hospital was used for evaluation.

In 2019, Shakeel, et.al., [22] have developed enhanced extensive DL and clustering quickly constructed neural networks to detect LC from CT images. Focuses on the quality enhancement of lung imaging to confirm the LC diagnosis without any misclassification. The dataset of the Cancer Imaging Archive was used to gather CT scans of the lungs. Using a weighted mean histogram equalization method, the noise in the images was successfully removed while also enhancing their quality. Segmentation of the affected regions was done by an enhanced method for extensive clustering. Various spectral data from the damaged regions are supplied into an immediately trained neural network in the DL environment to predict LC.

In 2021, Sori, et.al., [23] have suggested DL-based LC diagnosis from denoised CT scan images. DFD-Net, a two-path convolutional neural network with a "denoising first" architecture, was suggested as a solution to the lung cancer detection problem. The model has an end-to-end structure consisting of a denoising and a detection part. First, during preprocessing, noise is eliminated using DR-Net, a residual learning-based denoising network. The denoised image from DR-Net is fed into a two-path convolutional neural network to detect LC. The two branches help in joint embedding for both local and global features with the aid of using various receptive field sizes and help model local and global dependency. After, discriminant correlation analysis was introduced, which concatenates more representative features to improve model performance than previous techniques used for feature concatenation. At last, a retraining technique was introduced to handle image label imbalance problems.

In 2021, Xie, et.al., [24] have suggested machine learning methods to find early indicators for LC diagnosis. Forty-three healthy controls and 110 lung cancer patients in total were included. The amounts of sixty-one plasma metabolites were measured based on the targeted metabolomic analysis conducted with LC-MS/MS. The FCBF algorithm's top 5 metabolic biomarkers in terms of relative relevance may be beneficial as screening biomarkers for early LC diagnosis. Thus, it was suggested that Naïve Bayes be used as a useful technique for early LC prediction. As a result, this offers strong evidence in favor of the viability of blood-based screening and offers an enhanced, expedient, and comprehensive application tool for early lung cancer diagnosis. It may be possible to modify this multidisciplinary strategy for the extremely early diagnosis of malignancies other than LC.

In 2019, Sajja, et.al., [25] have suggested LC identification using deep transfer learning on CT scan data. In this case, a pre-trained CNN called GoogleNet served as the foundation for the building of a deep neural network. 60% of all neurons in the suggested network's tightly connected topology were placed on dropout layers to sparsify it to lower computing costs and avoid overfitting. The performance was tested using a pre-processed CT scan image dataset and the Lung Image Database Consortium dataset. This was contrasted with multiple CNNs that had already been trained. In comparison to the comparator networks, the recommended network performed better in terms of classification accuracy, according to the results.

In 2022, Shakeel, et.al., [26] have presented improved deep neural networks and ensemble classifiers used for LC identification from CT scans. In this case, a pre-trained CNN called GoogleNet served as the foundation for the building of a deep neural network. The proposed network was sparsified into a densely linked architecture with 60% of all neurons positioned on dropout layers to prevent overfitting and reduce processing expenses. The efficacy of the suggested network was assessed by a simulation that included a pre-processed CT scan image dataset from the Lung Image Database Consortium, LIDC, with numerous pre-trained CNNs, such as AlexNet, GoogleNet, and ResNet50.

The findings show that, when compared to comparison networks, the recommended network performed better in terms of classification accuracy.

In 2024, Gugulothu, et.al., [27] have presented a hybrid DL method for early detection of lung nodules using CT images. In these techniques, LNDC-HDL was suggested for CT imaging for the identification and categorization of lung nodules. First, it described an enhanced Fish Bee algorithm for selecting and extracting features; second, it explained a chaotic bird swarm optimization method for lung nodule division utilizing statistical information; and third, it proposed the HDENN algorithm, a hybrid classifier, for the classification and prognosis of tumors. Experimental results showed that the application of CT will improve the effectiveness and significance of the HDENN structure on the lung nodule detection performance in CT scans, increasing sensitivity and reducing false positives. The suggested method showed the effectiveness in HDENN node detection when applied in clinics.

PROPOSED METHODOLOGY

The different stages involved in the proposed LCD-CT-BiLSTM-RNN methodology for LC Detection are based on advancing CT Image analysis with hybrid BiLSTM-RNN. The lung CT images are first gathered from the dataset. After that, advanced image filtering techniques such as AGF are applied to decrease noise and balance edge-preserving smoothing for better image quality. Regions afflicted by cancer are segmented using AFKMC, which is sort of an enhanced version of the traditional K-means clustering algorithm integrated with fuzzy logic for flexibility and accuracy in results.
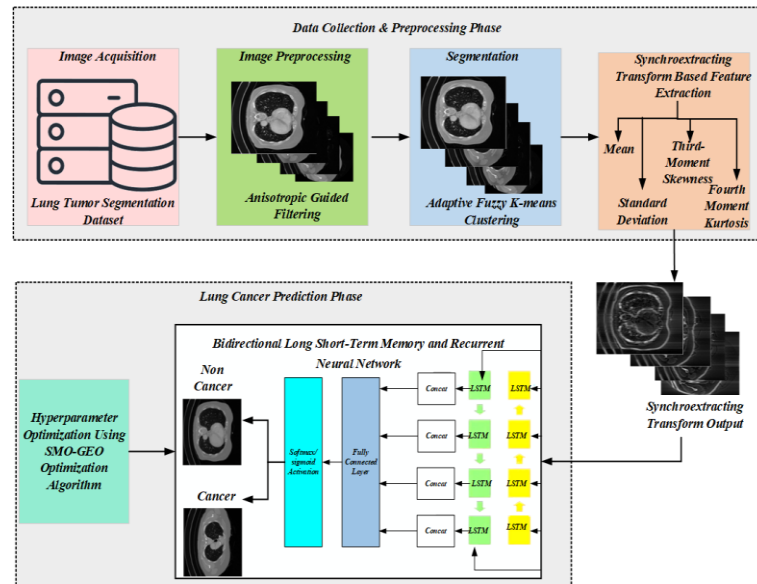

Figure 1: Block Diagram for Proposed LCD-CT-BiLSTM-RNN Methodology

This is followed by the application of Synchroextracting Transform to extract relevant patterns and spectral features from the segmented regions. BiLSTM is used to capture the contextual information of the previous and next time steps. This will be combined with RNNs, which process sequential data and maintain an internal memory of previous inputs, avoiding the problem of losing information on the sequential nature of data as typically experienced in traditional neural networks. It helps to ensure accurate and contextually informed classification results. A hybrid optimization technique consisting of SMO and GEO for fine-tuning the weight parameters of the BiLSTM-RNN is proposed. SMO is inspired by the foraging paths of slime molds, optimizing their efficiency, while GEO is based on how golden eagles hunt with adaptability and effectiveness in catching prey. The accuracy of lung cancer detection and classification between benign and malignant cases increases as a result of the weight parameters of BiLSTM-RNN being improved more effectively through the application of these techniques. For the suggested LCD-CT-BiLSTM-RNN approach, Figure 1 displays the block diagram.

Image Acquisition

Initially, the input images are taken from the Lung Tumor Segmentation Dataset [28]. This is a very varied dataset of CT scans acquired from patients with differential diagnoses of lung cancer. The dataset is drawn from multiple teams of medical centers and research projects about identifying and treating LC. The CT scan images make up the

majority of the dataset's content, which produces sectional visuals of the lungs. The CT images are stored in homogeneous clinical imaging formats, either DICOM format (Digital Imaging and Communications in Medicine) or NIfTI format (Neuroimaging Informatics Technology Initiative), to maintain the image quality and metadata information. The available segmentation masks are provided for each case of the CT scan. These are binary images in which the tumor area is outlined, and so they help in performing accurate segmentation. There can be several other types of noise that can contaminate the Lung Tumor Segmentation Dataset, damaging the quality and accuracy of the CT images. There may be Gaussian noise, which looks like random mathematical changes to pixel intensities due to the electronic intrinsic noise within the CT scanner itself. Then there is the Poisson noise due to statistical photon detection. The salt-and-pepper noise is engendered by black and white pixels, which are infrequent and pointedly spiky, probably because of errors in data transmission. This includes motion artifacts, produced by the patient's movement during the image acquisition process, and beam-hardening artifacts, manifested by streaks or shadows that extend outward from dense structures. Combined, all these kinds of noise degrade image clarity and may hamper the accurate segmentation and classification of lung tumors. Hence the input images undergo preprocessing in the next stage.

Image Preprocessing using Anisotropic Guided Filtering

The input CT scan images are then pre-processed by AGF [29]. It is a sophisticated filtering methodology applied to reduce noise and necessarily preserve the significant edges and details in the images. Then, anisotropic diffusion segregates the smoothing of homogeneous regions of the image without affecting the edges of the image. Thus, the quality of the CT scans can be enhanced. The preprocessing steps assure that high-quality images will output more accurate and reliable results in the segmentation and analysis stages that follow in order to identify and categorize lung cancers. Initially, create a vector out of the pixel values x_a given a patch from the input image that is indexed with the subscript a. This patch matches a different patch that was identical to the position in the reference images and vectorized to be called g_a. The averaging steps in equation (1) low-pass filter these values, whereas the formulation for I_a correctly adjusts the level of diffusion to reserve strong edges, thus nullifying these measurements. Due to weak diffusion when is little or excessive diffusion when is large, depending on the technique, details close to edges are either preserved or the edges dissolve. To obtain scaled images with dimensions, the resizing technique is first conducted to the input CT image samples it is demonstrated as follows in equation (1),

$$I_a = \sum_{b \in N(a)} w_{a,b} I_b$$

(1)

Where, $N(a)$ indicates the neighborhood of the pixel a, n denotes the number of pixels in the patch. To improve background removal, regularize the average step rather than J_a which is represented in equation (2),

$$J_a = \sum_{b \in N(a)} w_{ab} J_b$$

(2)

Where, w_{ab} denotes the importance attributed to a neighborhood situated at b the area around the pixel's center, which is at a. The objective in creating these weights is to accomplish maximum image cropping while maintaining distinct edge boundaries in the input image, which improves the input image's visual quality and is expressed as follows in equation (3),

$$\arg\min_{w_a} \quad J_a^2 + \mu \sum_{b \in N(a)} \left\| w_{ab} \Delta_b \right\|_2^2$$

(3)

Where, w_{ab} indicates how much weight is given to the neighborhood pixel b and Δ_b represents the neighborhood's gradients contained in a vector that is positioned in the reference image. Lastly, the segmentation procedure is given access to the pre-processed images.

Segmentation Using Adaptive Fuzzy K-means Clustering

In this section, the preprocessed input CT images are segmented using the AFKMC approach [30]. AFKMC is more appropriate in CT image segmentation due to the incorporation of conventional K-means and Fuzzy C-means clustering algorithms. This will assign every data point to its nearest cluster center; simultaneously, it allows fuzzy memberships so the data points lie in multiple clusters simultaneously. Basically, intends to reduce the difference between data points and cluster centers using fuzziness exponent. The position of the centroids is updated iteratively, based on a weighted average of all data points by their fuzzy memberships. This approach improves accuracy in clustering due to the introduction of belongingness, using a relationship between cluster centroids and their members as a metric. The process is iterated until convergence, which fosters optimal cluster assignments, and the CT images are then segmented accordingly. Its stepwise procedure is detailed as follows,

For the clustering of CT images, AFKMC must be used with the principles taken from traditional K-means and Fuzzy C-means algorithms. The objective function for AFKMC can be mathematically defined as in equation (4),

$$S = \sum_{l=1}^{n} \sum_{t=1}^{n} \left(W_{lt}^{w} \right) \left(u_t - d_l \right)^2$$

(4)

where W_{lt}^{w} represents the fuzzy membership function having fuzziness exponent w, quantifying the degree of membership of data point u_t to the cluster d_l. The centroid positions, d_l, get updated iteratively based on the equation (5),

$$d_l = \frac{\sum_{t=1}^{N} \left(W_{lt}^{w} \right) u_t}{\sum_{t=1}^{N} \left(W_{lt}^{w} \right)}$$

(5)

The following equation (6) calculates the new positions of centroids as a function of all the data, weighted by their fuzzy memberships.

$$C_l = \frac{d_l}{W_{lt}^{w}}$$

(6)

AFKMC improves clustering accuracy by introducing a measure of belongingness, hence reflecting the relation of cluster centroids with their members. The aforementioned iterative process is carried out until convergence is reached, thereby helping segment CT images through the minimization of the objective function, S.

Synchroextracting Transform-Based Features Extraction

In this section, the segmented images are fed to the Synchroextracting Transform (SET) to extract more relevant spectral features [31]. Equation (7) expresses the segmented images in a time-frequency representation based on the operation of the SET.

$$Z(s, f) = \int_{-\infty}^{\infty} z(\tau) \psi^* \left(\frac{\tau - s}{\lambda} \right) e^{-i2\pi f(\tau - s)} d\tau$$

(7)

Here, $Z(s, f)$ denotes the transform, $z(\tau)$ represents the preprocessed image at a time τ, ψ^* is the wavelet function under analysis's complex conjugate, s is the time parameter, f is the frequency parameter, and λ is the

scale parameter. This transform maps the image into a 2D representation in the temporal-frequency domain, indicating how the entire image's content is distributed over these different time and frequency components. From this representation, many spectral features, including the mean, standard deviation, skewness of the third moment, and kurtosis of the fourth moment can be further derived to provide a better description of the structural and patterned information of the image. These features capture different statistical properties of the pixel intensity values, hence providing important information for accurate classification. The estimated spectral features are represented as follows,

Mean (μ)

The mean in the segmented area is the pixel's average intensity value. It is used to measure the overall brightness of the area. The formula for the mean is calculated using the equation (8),

$$\mu = \frac{1}{n}\sum_{a=1}^{n} S_a$$

(8)

Where, n is the total quantity of pixels in the segmented region, and S_a represents the intensity of the ath pixel.

Standard Deviation (σ)

It is the measure of dispersion or spread of pixel intensity values around the mean. It gives information regarding the amount of variation in the intensity values within a segmented region. The formula for the standard deviation is provided in Equation (9),

$$\sigma = \sqrt{\frac{1}{n}\sum_{a=1}^{n}\left(S_a - l\right)^2}$$

(9)

Where, l is the mean intensity value.

Third-Moment Skewness (SK)

The asymmetry in the distribution of pixel intensity is known as skewness. A distribution with a long tail to the right will be positively skew, while a distribution with a long tail to the left will be negatively skew. The formula for skewness is represented in equation (10),

$$SK = \left(\frac{1}{n\sigma^3}\sum_{a=1}^{n}\left(S_a - l\right)^3\right)^{1/3}$$

(10)

Fourth Moment Kurtosis (KU)

Kurtosis quantifies how flat or peaky the distribution of pixel intensity is about the normal distribution. High kurtosis denotes a strong peak, while low kurtosis denotes a flat distribution. The formula for kurtosis is represented in equation (11)

$$KU = \left(\frac{1}{n\sigma^4}\sum_{a=1}^{n}\left(S_a - l\right)^4\right)^4$$

(11)

Where, σ is the standard deviation and l is the mean intensity value. These spectral patterns offer important new information about the properties of the lung tissue seen in CT scans. With the highest degree of accuracy, lung areas can be classified as malignant or non-cancerous by examining these traits.

Lung Cancer Classification Using BiLSTM-RNN

In this section, the extracted features are fed into the architecture of the BiLSTM-RNN model for LC classification. The input layer consists of extracted medical data features relevant to lung disease classification. The BiLSTM [32]

deals with the challenge of learning to process sequential data in both forward and backward directions to identify long-term dependencies simultaneously. This can be further made possible due to its complex structure with memory cells and three essential gates: input, output, and forget. These gates thus control the amount of information passed through the network and, hence, let the Bi-LSTM retain class-relevant information about a task, such as the classification of lung diseases based on integrated patient data. This understanding ability, therefore, effectively handles subtle temporal patterns across long sequences, hence becoming an effective tool for those tasks that require a strong understanding of sequential medical data. RNN [33] model contributes to retaining a memory state that helps retain sequential information, though with flaws such as the vanishing gradient problem. By combining BiLSTM and RNN, the model can leverage the strengths of both architectures. BiLSTM excels in capturing long-term dependencies and context while RNN helps in processing sequential information efficiently. Hybrid models often exhibit reduced overfitting compared to single-model approaches, as they can generalize better by integrating diverse learning mechanisms. Initially, the amount of additional data that should be added to the cell state from the present input is determined by input gate I_t and is represented in equation (12),

$$I_t = \sigma\left(W_I \cdot \left[H_{t-1}, x_t\right] + b_I\right)$$

(12)

The forget gate decides what information from the previous cell state should be ignored or remembered. Additionally, it is stated in equation (13).

$$F_t = \sigma\left(W_F \cdot \left[H_{t-1}, x_t\right] + b_F\right)$$

(13)

The output gate controls the amount of information that is sent from the current cell state to the next hidden state which is represented mathematically in equation (14),

$$O_t = \sigma\left(W_O \cdot \left[H_{t-1}, x_t\right] + b_O\right)$$

(14)

Equation (15) is then used to obtain the cell update state, which updates the cell state by incorporating the new information from both the previous and the input state from the forget gate.

$$\hat{C}_t = \tanh\left(W_C \cdot \left[H_{t-1}, x_t\right] + b_C\right)$$

(15)

The cell state is updated according to the results obtained from both the forget and input gates, hence capturing a long-term dependency using equation (16)

$$C_t = F_t \cdot C_{t-1} + i_t \cdot \hat{C}_t$$

(16)

The cell state is transmitted to the following LSTM unit and the output gate modifies the hidden state which is expressed in equation (17) as follows,

$$H_t = O_t \cdot \tanh\left(C_t\right)$$

(17)

Concatenation is performed on the forward and reverse LSTM outputs to form one integrated representation of the data which is exhibited in equation (18),

$$H_t^{bi} = \left[\vec{h}_t; \overleftarrow{h}_t\right]$$

(18)

Where, $\vec{h}_t$ indicates the forward LSTM output and $\overleftarrow{h}_t$ denotes the backward LSTM output. Then the output from the BiLSTM layer is concatenated and fed into an RNN layer for further forward propagation processing. This layer performs the processing of the combined features to learn associations and dynamics in the serial data over time. At the initial timestep $t=0$ set the initial hidden state to zeros. For subsequent timesteps, $t>0$ the hidden state is updated as expressed in the equation (19),

$$H_t = \sigma\left(W_H \cdot H_{t-1} + W_x \cdot H_t^{bi} + b\right)$$

(19)

In the output layer, at the initial time step $t = 0$ initialize the output as zero and for the subsequent time steps $t > 0$ the output is computed using equation (20) as follows,

$$Y_t = \phi\left(W_Y \cdot H_t + C\right)$$

(20)

The RNN layer increases the ability of the model to capture complex dependency structures that span across the entire sequence of features of medical data. The hidden state H_t is updated based on the current input H_t^{bi} and the previous hidden state H_{t-1}, using weights W_H and W_x and bias b. The output Y_t is processed through an activation function ϕ, such as softmax for lung cancer classification. Then feed the developed features from the RNN layer into a fully connected layer, which can combine learned features in the development of complex representations concerning the lung disease state. The results that come as an output from the fully connected layer are then sent through an activation function to compute the final class predictions. To improve the suggested model's performance the weight parameters W_H, W_x, and W_Y of the BiLSTM-RNN are tuned using the SMO-GEO optimization algorithm.

Stepwise Procedure of SMO-GEO Optimization Algorithm

The combination of SMO [34] with the GEO [35] algorithm results in a more powerful hybrid optimization technique, SMO-GEO, for the tuning of weight parameters W_H, W_x, and W_Y of the BiLSTM-RNN mode. In that manner, it derives the power of both SMO and GEO to achieve optimized convergence and improved accuracy for disease classification related to the lungs. Slime Mould Optimization is inspired by foraging behavior in slime moulds, in which he optimizes his path to find food. SMO is effective for searching the search area and obtains the global optimality by simulation of the oscillatory behavior of slime moulds. Important salient features of SMO are: (i) Searches the search space by simulation of the oscillatory behavior of slime moulds. (ii) Achieves a balance between exploration and exploitation through adaptive changes in search behavior. (iii) Appropriate for multi-modal optimization problems with complex natures. The GEO algorithm is motivated by the prey-hunting behavior of the Golden Eagles. Key points of GEO focus on the exploitation of the search space by converging on the promising regions. The GEO imitates the strategy of eagle hunting through identification and convergence on the prey, which is useful in exploiting the promising regions of the search space. It balances exploration and exploitation and provides adaptive tuning of parameters. Effective at fine-tuning solutions to carry out in the most optimum way. In particular, the proposed SMO-GEO approach encompasses the exploring capability of SMO and exploiting the strength of GEO, hereby forming a comprehensive optimization framework in tuning the weight parameters of the BiLSTM-RNN model. Its stepwise procedures are represented as follows,

Step 1: Initialization

In this step initialize the population of weight parameters W_H, W_x, and W_Y for the BiLSTM-RNN model.

Step 2: Random Generation

selects, after initialization, at random, the best response from the initialized input parameter.

Step 3: Fitness Function

Here, optimizing the weight parameters W_H, W_x, and W_Y from the BiLSTM-RNN approach serves as the goal function. Its description is represented in equation (21),

$$Fitness\ Function = Optimization\left[W_H, W_x, and\ W_Y\right]$$

(21)

Step 4: Approach the SMO Food

Food may be approached by slime mould based on environmental smells. The contraction mod's approaching mathematical behavior, shown in equation (18), is approximated by the following formulas:

$$\overrightarrow{B(s+1)} = \begin{cases} \overrightarrow{B_y(s)} + \overrightarrow{vy}.\left(\vec{T}.\,\overrightarrow{B_X(s)} - \overrightarrow{B_Y(s)}\right), & w < q \\ \overrightarrow{vz}.\overrightarrow{B(s)}, & w \geq q \end{cases}$$

(22)

Whereas, $\overrightarrow{vy}$ the parameter has a range of $[-a,a]$, $\overrightarrow{vz}$ decreases linearly from one to zero, s denotes the current iteration, $\vec{B}_Y$ designates the specific location where the odor concentration is highest at that moment, $\vec{B}$ shows the location of the slime mold, $\vec{B}_X$ and $\vec{B}_Y$ designate the individuals selected at random from a slime mold. The weight of the slime mold is represented by $\vec{T}$. Equation (23) represents the q formula.

$$q = \tanh\left|R(i) - BF\right|$$

(23)

where the fitness of $\vec{B}$ is represented by $i \in 1, 2, \ldots, n$, $R(i)$ and the best fitness attained throughout all iterations is represented by BF. The following is the formula for $\overrightarrow{vy}$,

$$\overrightarrow{vy} = [-a, a]$$

(24)

$$a = \arctan h\left(-\left(\frac{s}{\max\_s}\right) + 1\right)$$

(25)

The following equation (26) is a list of the formulas for $\vec{T}$,

$$T\left(Smellindex(i)\right) = \begin{cases} 1 + w.\log\left(\dfrac{oF - R(i)}{oF - wF} + 1\right), & If\ R(i) > half\ of\ the\ population \\ 1 - w.\log\left(\dfrac{oF - R(i)}{oF - wF} + 1\right), & others \end{cases}$$

(26)

Within the current cycle of iterations, w symbolizes the random value falling inside the [0,1] range, oF shows the best fitness value that is attained, wF shows the lowest fitness level attained, and $Smellindex$ shows the order in which the fitness values have been sorted (ascending in the lowest value problem) and is computed using equation (27),

$$Smellindex(i) = Sort(R)$$

(27)

Step 5: Attack (Exploitation) of GEO

The attack can be represented as a vector that terminates at the prey's location in the golden eagle's memory and begins at its current location. Equation (28) is used to calculate it.

$$\overrightarrow{E_i} = \overrightarrow{X_f^*} - \overrightarrow{X_i}$$

(28)

Where, $\overrightarrow{E_i}$ indicates the eagle's attack vector, $\overrightarrow{X_f^*}$ represents the finest place (prey) the eagle has visited thus far f, $\overrightarrow{X_i}$ indicates the eagle's present location i. The attack vector draws attention to the exploitation stage in GEO since it concentrates the golden eagle population in the most visited areas.

$$q = \tanh \vec{E} \left| R(i) - BF \right|$$
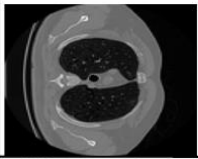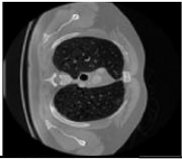
(29)
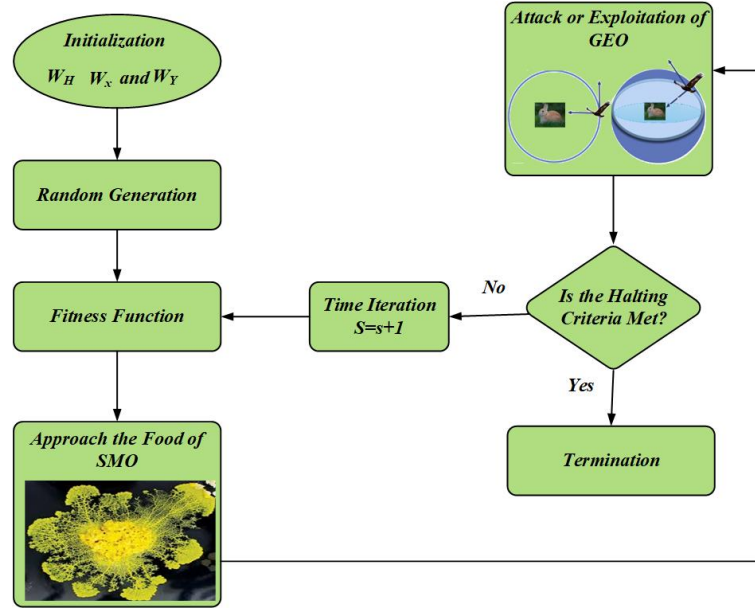
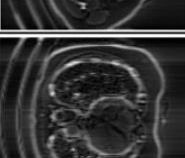Figure 2: Flowchart of SMO-GEO Algorithm
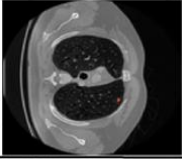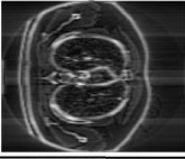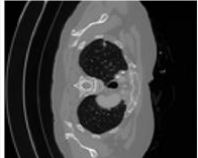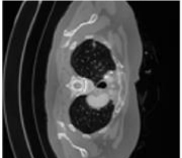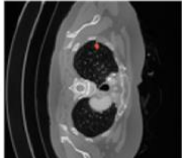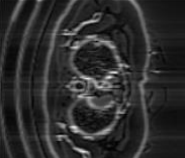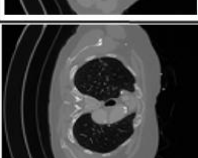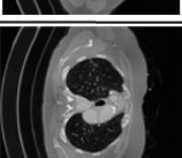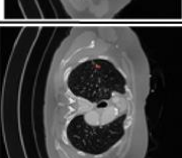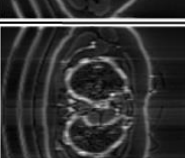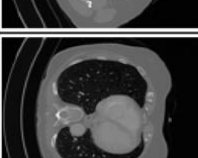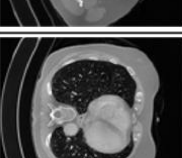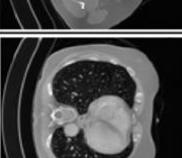
Step 6: Termination

Proceed to step 3 of the procedure if the stopping criteria are not met. If $s = s + 1$ is reached, the maximum iteration will cease. The flowchart of SMO-GEO is displayed in Figure 2. At last, the weight parameters W_H, W_x, and W_Y of the BiLSTM-RNN are tuned more efficiently and provide the final classification outcome as cancer or non-cancer with higher accuracy.

RESULT AND DISCUSSION

This section discusses the simulation findings for the proposed LCD-CT-BiLSTM-RNN approach. Traditional methods such as FPSO-CNN, DITNN-IPCT, and DR-Net-CNN were used in simulations on MATLAB to show the superiority and efficacy of the proposed LCD-CT-BiLSTM-RNN approach. Here the performance measures such as Accuracy, Specificity, Sensitivity, Precision, Recall, ROC, F-1 Score, and MCC are analyzed. Table 1 outlines the output result of the proposed LCD-CT-BiLSTM-RNN approach.

Table 1: Output Result of Proposed LCD-CT-BiLSTM-RNN Approach

Performance Measures

In this instance, performance metrics like ROC, F1-score, MCC, Accuracy, Specificity, Sensitivity, Precision, Recall, and F1-score are utilized to assess how effective the recommended course of action is. They are listed below:

Accuracy

It calculates the entire expected accuracy of the model while accounting for real positives and negatives. It's computed by applying equation (30).

$$Accuracy = \left(\frac{TP + TN}{TP + TN + FP + FN} \right)$$

(30)

Sensitivity/Recall

The percentage of positive results that the model accurately and consistently predicts is measured by sensitivity. Equation (31) is used for the calculation,

$$Sensitivity / \mathrm{Re}\,call = \left(\frac{TP + TN}{FN} \right)$$

(31)

Precision

The precision of the proposed model is defined as the percentage of all positive forecasts that are accurate. To calculate it, use equation (32),

$$\mathrm{Pr}\,ecision = \left(\frac{TP}{TP + FP} \right)$$

(32)

Specificity

Specificity is measured by equation (33), which indicates how well the recommended approach detects undesired events.

$$Specificity = \left(\frac{TN}{TN + FP} \right)$$

$$(33)$$

F1-score

The harmonic mean of recall and precision is shown in the F1-score. Equation (34) is used to compute it as follows:

$$F1 - score = 2 * \left(\frac{\Pr ecision * \operatorname{Re} call}{\Pr ecision + \operatorname{Re} call} \right)$$

$$(34)$$

Matthews Correlation Coefficient (MCC)

All four values (TP, TN, FP and FN) are considered by MCC, this yields a single result that accounts for both over- and under-prediction and represents the model's efficacy. To calculate it, use equation (35).

$$MCC = \frac{(TP * TN - FP * FN)}{\sqrt{((TP + FP) * (TP + FN) * (TN + FP) * (TN + FN))}}$$

$$(35)$$

Comparison Results of the Proposed Model with Existing Methods

Figure 3-11 displays the outcomes of the suggested approach's simulation. Here, the suggested LCD-CT-BiLSTM-RNN strategy's efficacy is contrasted with that of existing methods including FPSO-CNN, DITNN-IPCT, and DR-Net-CNN.
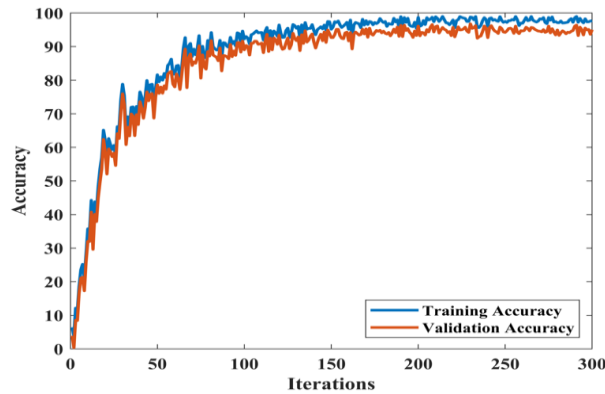

Figure 3: Training and Validation Accuracy Plot

The training and validation accuracy of a 300-iteration lung cancer detection model is shown in Figure 3. The accuracy is displayed as a % on the y-axis, and the number of iterations is represented by the x-axis. Training accuracy is expressed by the blue line, first is low, but increases rapidly to get above 50% after about the 25th iteration. The accuracy is also seen to increase monotonically, with some fluctuations, eventually stabilizing at almost 100% accuracy by the 300th iteration. The validation accuracy follows a similar pattern to the training accuracy, starting low and increasing rapidly before leveling off. From the 300th iteration onward, which is generally inclusive of minor ups and downs, this only rises steadily to stabilize at around 90% accuracy. It proves that the model can learn quite effectively during training itself, since it achieves high accuracy on both the validation and training datasets. The lines for training and validation accuracy are very much alike, which means that the model fits quite nicely to unseen data and there is no significant overfitting. This result is really very important for guaranteeing the reliability and resilience of the lung cancer detection system.
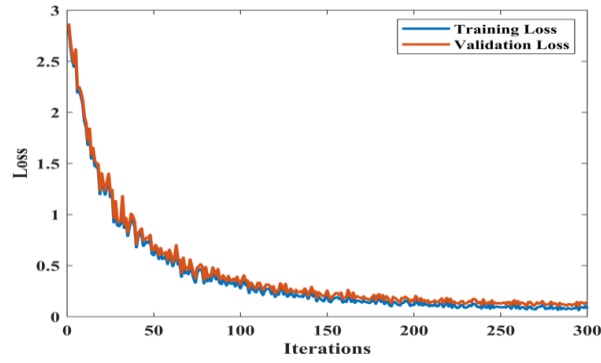
Figure 4: Training and Validation Loss Plot

The training and validation losses of a lung cancer detection model across 300 iterations are shown in Figure 4. Iterations are plotted on the x-axis, and loss values are displayed on the y-axis. Beginning at very high values of around 2.8 for both the training and the validation losses, the graph drops rapidly within the first 50 iterations. This steep fall was then followed by a gradual reduction where, by the 300th iteration, both losses were around 0.1. The training and validation loss curves' tight adherence indicates that the model is learning effectively with little overfitting, which will lead to an improvement in its ability to detect lung cancer with accuracy.
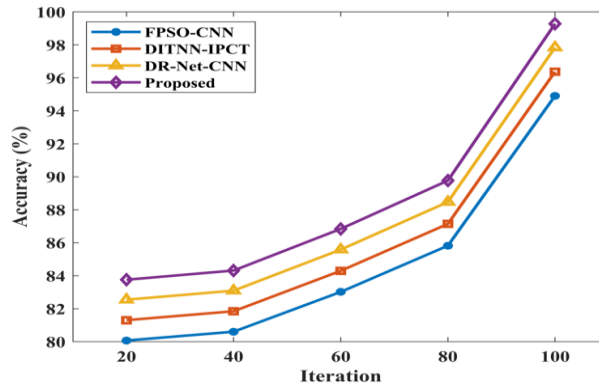

Figure 5: Accuracy Analysis

The accuracy analysis is shown in Figure 5. Here, the performance of the proposed LCD-CT-BiLSTM-RNN method outperforms the current models, FPSO-CNN, DITNN-IPCT, and DR-Net-CNN, respectively, by 2.06%, 4.13%, and 3.22% for iteration 20; 3.24%, 1.97%, 2.74% higher accuracy for iteration 40; 1.72%, 3.16%, 2.44% higher accuracy for iteration 60; 2.74%, 3.34%, and 1.77% higher accuracy for iteration 80; 5.69%, 10.52%, and 8.14% higher accuracy for iteration 100.
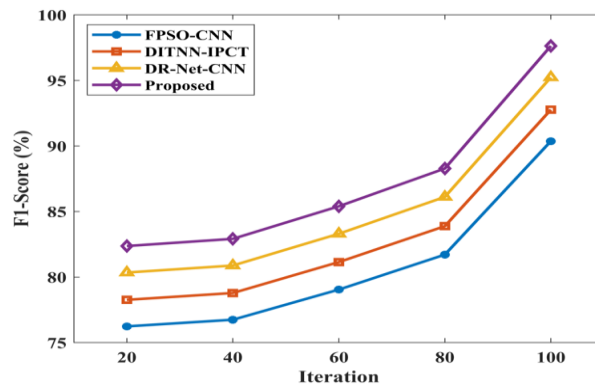

Figure 6: F1-Score Analysis

In Figure 6, the F1-Score analysis is shown. In this case, the suggested LCD-CT-BiLSTM-RNN method's performance offers 3.10%, 3.21%, and 1.03% higher F1-Score for iteration 20; 1.23%, 3.18%, and 2.56% higher F1-Score for iteration 40; 4.87%, 6.34%, and 3.77% higher F1-Score for iteration 60; 5.15%, 3.18%, and 1.21% higher F1-Score for

iteration 80; 1.53%, 3.31%, 4.91% higher F1-Score for iteration 100 compared with existing models FPSO-CNN, DITNN-IPCT, and DR-Net-CNN respectively.
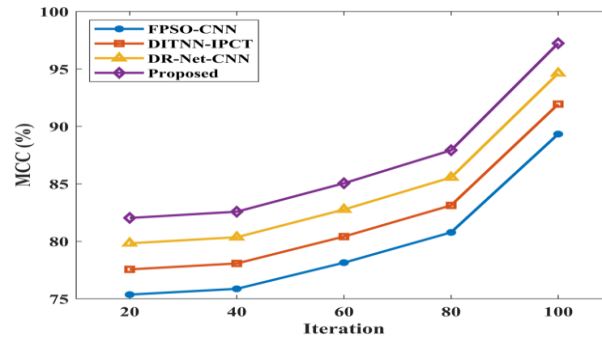

Figure 7: MCC Analysis

Figure 7 displays the MCC analysis. The results indicate that the LCD-CT-BiLSTM-RNN method performs better than the existing models FPSO-CNN, DITNN-IPCT, and DR-Net-CNN by 2.27%, 3.51%, 3.18%, 2.47%, 3.01%, 4.55%, higher MCC for iteration 20, 6.2%, 2.27%, 4.08%, higher MCC for iteration 60, 1.79%, 4.73%, 1.41% higher MCC for iteration 80, and 3.21%, 4.18%, 1.51% higher MCC for iteration 100.
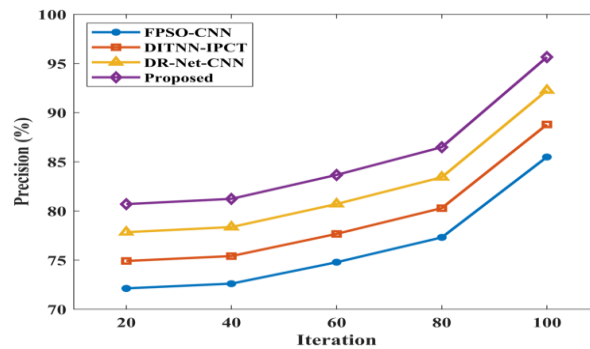

Figure 8: Precision Analysis

The precision analysis is displayed in Figure 8. In this case, the performance of the suggested LCD-CT-BiLSTM-RNN method outperforms the current models FPSO-CNN, DITNN-IPCT, and DR-Net-CNN, respectively, by 3.02%, 2.58%, and 5.98% for iteration 20; 3.45%, 4.35%, and 6.88% for iteration 40; 4.25%, 6.70%, and 2.98% for iteration 60; 3.72%, 5.23%, and 2.12% for iteration 80; 1.28%, 2.02%, and 5.02% higher precision for iteration 100.
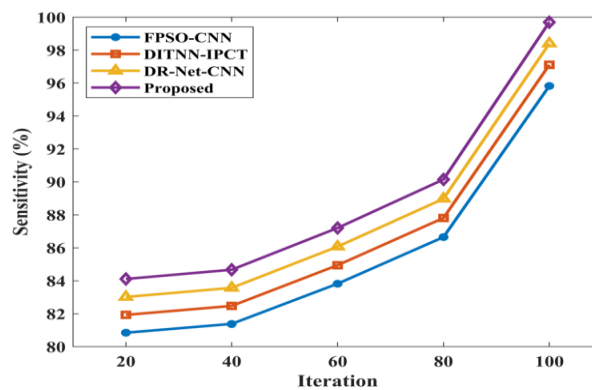

Figure 9: Sensitivity Analysis

The sensitivity analysis is displayed in Figure 9. The results indicate that the LCD-CT-BiLSTM-RNN method outperforms the current models FPSO-CNN, DITNN-IPCT, and DR-Net-CNN by 5.25%, 9.67%, and 7.55% for iteration 20; 3.02%, 2.78%, and 5.54% higher sensitivity for iteration 40; 2.08%, 8.08%, and 9.02% higher sensitivity for iteration 60; 5.09%, 3.97%, and 4.05% higher sensitivity for iteration 80; 5.72%, 6.74%, and 8.32% higher sensitivity for iteration 100.
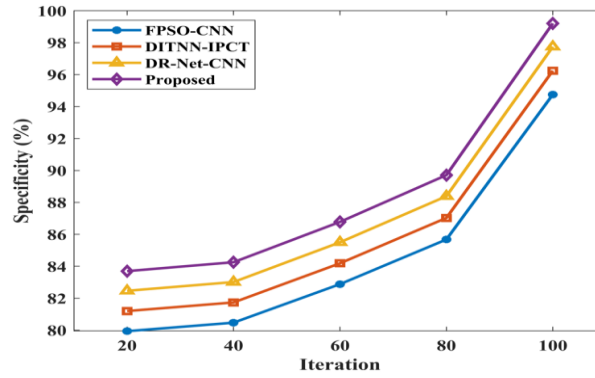
Figure 10: Specificity Analysis

The specificity analysis is displayed in Figure 10. In comparison to the existing models, FPSO-CNN, DITNN-IPCT, and DR-Net-CNN, respectively, the performance of the proposed LCD-CT-BiLSTM-RNN method yields 5.85%, 7.25%, and 8.78% higher specificity for iteration 20; 3.89%, 5.35%, and 8.25% higher specificity for iteration 40; 6.87%, 8.35%, and 2.78% higher specificity for iteration 60; 7.02%, 3.85%, and 4.35% higher specificity for iteration 80; 9.25%, 2.47%, and 4.95% higher specificity for iteration 100.
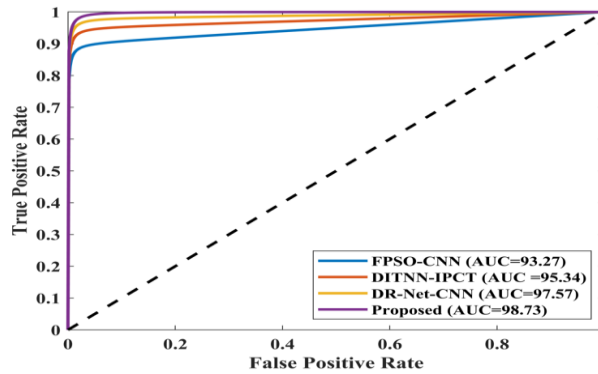

Figure 11: Receiver Operating Characteristic Curve (ROC) Analysis

Figure 11 displays the ROC analysis. In this instance, the suggested LCD-CT-BiLSTM-RNN approach outperforms the current models FPSO-CNN, DITNN-IPCT, and DR-Net-CNN, yielding 1.85%, 1.52%, and 2.14% higher AUC, respectively.

CONCLUSION

In this manuscript, LC detection based on advancing CT image analysis through hybrid BiLSTM-RNN is implemented successfully. In the proposed method of LCD-CT-BiLSTM-RNN, multiple advanced techniques have been embedded to improve its accuracy in detecting lung cancer. AGF anisotropic guided filtering may be applied to reduce noise in lung CT images, while AFKMC is used for accurate segmentation of cancer-affected areas. SET will be applied to enhance robust spectral feature extraction. This manuscript has therefore been focused on the hybrid BiLSTM and RNN architecture fine-tuned by Slime Mould Optimization and Golden Eagle optimization to have better classification. The comparative analysis performed in MATLAB shows that the proposed method outperforms other state-of-the-art techniques such as FPSO-CNN, DITNN-IPCT, and DR-Net-CNN by 1.47%, 3.21%, and 2.42% in terms of MCC. All comprehensive evaluation metrics, including accuracy, precision, recall, F1-score, specificity, and ROC, validate this proposed technique for the improvement of lung cancer detectability from a CT image. Future work will focus on IoT-based multiclass classification could involve improving data acquisition and integration from the various IoT devices, including wearable sensors and smart home systems, toward real-time and continuous patient monitoring. Explore attention-based transformers and graph neural networks as advanced deep learning models for better grasping of the difficult interdependencies within multimodal data. Moreover, federated learning can be deployed to enhance the generalizability of models in the presence of patient privacy. Next, such strong optimization techniques, made possibly with the help of quantum computing, would come in place to apply the models for effective and efficient training. For all these applications, real-world testing concerning the applicability and reliability of the proposed solution is pivotal.

REFERENCES

[1] Faruqui, N. et al. (2021) 'LungNet: A hybrid deep-CNN model for lung cancer diagnosis using CT and wearable sensor-based medical IOT Data', Computers in Biology and Medicine, 139, p. 104961.

[2] Kumar, R. et al. (2021) 'An integration of blockchain and AI for secure data sharing and detection of CT images for the Hospitals', Computerized Medical Imaging and Graphics, 87, p. 101812.

[3] Talukder, Md.A. (2022) Machine learning-based lung and colon cancer detection using deep feature extraction and Ensemble Learning [Preprint].

[4] Ibrahim, D.M., Elshennawy, N.M. and Sarhan, A.M. (2021) 'Deep-chest: Multi-classification deep learning model for diagnosing COVID-19, pneumonia, and lung cancer chest diseases', Computers in Biology and Medicine, 132, p. 104348.

[5] Tian, Q. et al. (2021) 'A new optimized sequential method for lung tumor diagnosis based on deep learning and converged search and rescue algorithm', Biomedical Signal Processing and Control, 68, p. 102761.

[6] Shanthi, S. and Rajkumar, N. (2020) 'Lung cancer prediction using Stochastic Diffusion Search (SDS) based feature selection and Machine Learning Methods', Neural Processing Letters, 53(4), pp. 2617–2630.

[7] Pradhan, K., Chawla, P. and Rawat, S. (2022) 'A deep learning-based approach for detection of lung cancer using self adaptive sea lion optimization algorithm (SA-SLNO)', Journal of Ambient Intelligence and Humanized Computing, 14(9), pp. 12933–12947.

[8] Gould, M.K. et al. (2021) 'Machine learning for early lung cancer identification using routine clinical and laboratory data', American Journal of Respiratory and Critical Care Medicine, 204(4), pp. 445–453.

[9] Faruqui, N. et al. (2021) 'LungNet: A hybrid deep-CNN model for lung cancer diagnosis using CT and wearable sensor-based medical IOT Data', Computers in Biology and Medicine, 139, p. 104961.

[10] Marentakis, P. et al. (2021) 'Lung cancer histology classification from CT images based on radiomics and Deep Learning Models', Medical & Biological Engineering & Computing, 59(1), pp. 215–226.

[11] Riquelme, D. and Akhloufi, M. (2020) 'Deep learning for lung cancer nodules detection and classification in CT scans', AI, 1(1), pp. 28–67.

[12] Guo, Z., Xu, L., Si, Y. and Razmjooy, N., 2021. Novel computer-aided lung cancer detection based on convolutional neural network-based and feature-based classifiers using metaheuristics. International Journal of Imaging Systems and Technology, 31(4), pp.1954-1969.

[13] Sujitha, R. and Seenivasagam, V. (2020) 'Classification of Lung Cancer Stages with machine learning over Big Data Healthcare Framework', Journal of Ambient Intelligence and Humanized Computing, 12(5), pp. 5639–5649.

[14] P., S. and M., P.B. (2021) 'Diagnosis of lung cancer using hybrid deep neural network with adaptive sine cosine crow search algorithm', Journal of Computational Science, 53, p. 101374.

[15] Ubaldi, L. et al. (2021) 'Strategies to develop radiomics and machine learning models for lung cancer stage and histology prediction using small data samples', Physica Medica, 90, pp. 13–22.

[16] Doppalapudi, S., Qiu, R.G. and Badr, Y. (2021) 'Lung cancer survival period prediction and understanding: Deep Learning Approaches', International Journal of Medical Informatics, 148, p. 104371.

[17] Murugesan, M. et al. (2022) 'A hybrid deep learning model for effective segmentation and classification of lung nodules from CT images', Journal of Intelligent & Fuzzy Systems, 42(3), pp. 2667–2679.

[18] Bębas, E. et al. (2021) 'Machine-learning-based classification of the histological subtype of non-small-cell lung cancer using MRI texture analysis', Biomedical Signal Processing and Control, 66, p. 102446.

[19] Nair, J.K. et al. (2020) 'Radiogenomic models using machine learning techniques to predict EGFR mutations in non-small cell lung cancer', Canadian Association of Radiologists Journal, 72(1), pp. 109–119.

[20] Mikhael, P.G. et al. (2023) 'Sybil: A validated Deep Learning model to predict future lung cancer risk from a single low-dose chest computed tomography', Journal of Clinical Oncology, 41(12), pp. 2191–2200.

[21] Asuntha, A. and Srinivasan, A., 2020. Deep learning for lung Cancer detection and classification. Multimedia Tools and Applications, 79, pp.7731-7762.

[22] Shakeel, P.M., Burhanuddin, M.A. and Desa, M.I., 2019. Lung cancer detection from CT image using improved profuse clustering and deep learning instantaneously trained neural networks. Measurement, 145, pp.702-712.

[23] Sori, W.J., Feng, J., Godana, A.W., Liu, S. and Gelmecha, D.J., 2021. DFD-Net: lung cancer detection from denoised CT scan image using deep learning. Frontiers of Computer Science, 15, pp.1-13.

[24] Xie, Y., Meng, W.Y., Li, R.Z., Wang, Y.W., Qian, X., Chan, C., Yu, Z.F., Fan, X.X., Pan, H.D., Xie, C. and Wu, Q.B., 2021. Early lung cancer diagnostic biomarker discovery by machine learning methods. Translational oncology, 14(1), p.100907.

[25] Sajja, T., Devarapalli, R. and Kalluri, H., 2019. Lung Cancer Detection Based on CT Scan Images by Using Deep Transfer Learning. Traitement du Signal, 36(4), pp.339-344.

[26] Shakeel, P.M., Burhanuddin, M.A. and Desa, M.I., 2022. Automatic lung cancer detection from CT image using improved deep neural network and ensemble classifier. Neural Computing and Applications, pp.1-14.

[27] Gugulothu, V.K. and Balaji, S., 2024. An early prediction and classification of lung nodule diagnosis on CT images based on hybrid deep learning techniques. Multimedia Tools and Applications, 83(1), pp.1041-1061.

[28] https://www.kaggle.com/datasets/pypiahmad/lung-tumor-data

[29] Ochotorena, C.N. and Yamashita, Y. (2020) 'Anisotropic guided filtering', IEEE Transactions on Image Processing, 29, pp. 1397–1412.

[30] Chen, L. et al. (2020) 'Single-cell transcriptome data clustering via multinomial modeling and adaptive fuzzy K-means algorithm', Frontiers in Genetics, 11.

[31] Dong, H. and Yu, G. (2022) 'Comments on "synchroextracting transform: The theory analysis and comparisons with the synchrosqueezing transform"', Signal Processing, 190, p. 108345.

[32] Mei, S. et al. (2022) 'Hyperspectral image classification using attention-based bidirectional long short-term Memory Network', IEEE Transactions on Geoscience and Remote Sensing, 60, pp. 1–12.

[33] Wang, Y. et al. (2023) 'PredRNN: A recurrent neural network for spatiotemporal predictive learning', IEEE Transactions on Pattern Analysis and Machine Intelligence, 45(2), pp. 2208–2225.

[34] Li, S. et al. (2020) 'Slime mould algorithm: A new method for stochastic optimization', Future Generation Computer Systems, 111, pp. 300–323.

[35] Mohammadi-Balani, A. et al. (2021) 'Golden Eagle Optimizer: A nature-inspired metaheuristic algorithm', Computers &amp; Industrial Engineering, 152, p. 107050.